



1 Curved atmospheric rivers and their moisture remnants: a new 2 detection tool for Antarctica

3 Victoire Buffet^{1,2}, Vincent Favier¹, Benjamin Pohl², Jonathan D. Wille¹

4 ¹Université Grenoble Alpes/CNRS/IRD/G-INP, IGE, Grenoble, 38000, France

5 ²Biogéosciences, UMR6282 CNRS / Université Bourgogne Europe, Dijon, 21000, France

6 *Correspondence to:* Victoire Buffet (victoire.buffet@univ-grenoble-alpes.fr)

7 **Abstract.** Atmospheric rivers (ARs) represent the main intrusions of moisture and heat into Antarctica, exerting a major
8 influence on the continent's surface mass balance. Yet, due to geometric and directional constraints, existing detection
9 algorithms often fail to track their evolution inland after landfall or in regions where abrupt directional changes occur. We
10 introduce DARK (Detecting ARs using their Kurvature), a new Antarctic AR detection framework designed to overcome these
11 limitations. DARK applies a strict 98th-percentile threshold to total integrated vapor transport and computes AR length along
12 the curved axis to evaluate the 2000-km AR criterion. This enables the continuous detection of ARs with complex geometries,
13 including those that curve, overturn, or extend across the South Pole. An additional AR-children module identifies smaller but
14 still intense moisture remnants that detach from parent ARs after landfall yet continue to transport vapor and heat inland. The
15 resulting climatology shows that DARK ARs account for about 18 % of total Antarctic precipitation and are linked to roughly
16 half of top 1 % daily precipitation anomalies, 60 % of top 1 % daily maximum temperature anomalies, and 80 % of compound
17 warm-and-wet events. DARK provides a more detailed assessment of AR-related precipitation and temperature impacts in the
18 South Pole region. Despite slightly higher occurrence, risk ratio analysis shows that DARK ARs more effectively capture the
19 most intense events than earlier Antarctic schemes. Including AR-children further strengthens these associations, especially
20 over Victoria Land, where they contribute to about one third of AR-related precipitation.

21

22

23

24

25

26

27

28

29



30 **Plain Language Summary.** Atmospheric rivers (ARs) are long, narrow corridors of air that transport large amounts of water
31 vapor and heat from lower latitudes into Antarctica. These events play a major role in shaping Antarctic weather and the ice
32 sheet's mass balance, but many current detection methods struggle to track them accurately as they move inland. We developed
33 a new method, called DARK (Detecting Atmospheric Rivers using their Kurvature), that can identify and follow atmospheric
34 rivers with complex shapes, including those that curve or cross the South Pole. The method also detects smaller features, called
35 "AR-children", which break away from larger systems but continue to carry moisture and warmth inland. Our results show
36 that ARs detected by DARK contribute to about 18 % of all Antarctic precipitation and are linked to many extreme events,
37 including half of the most intense daily precipitation, 60 % of high temperature days, and 80 % of events that are both warm
38 and wet. Including the smaller AR-children further strengthens these associations, particularly in regions such as Victoria
39 Land. Although part of this increase reflects the larger number of detected ARs, risk ratio analysis shows that DARK ARs are
40 equally or more effective at capturing these intense anomalies. This framework provides a more complete understanding of
41 AR-driven processes that influence the Antarctic Ice Sheet.

42

43

44 **Keywords :** Atmospheric rivers – Antarctica – Precipitation – Detection tool – Methodology

45 **1 Introduction**

46 Atmospheric rivers (ARs) are long, narrow filaments of enhanced horizontal water vapor transport that are an essential
47 component of the global hydrological cycle and particularly play a central role in the Antarctic surface mass balance (Zhu and
48 Newell, 1998). ARs contribute positively to the Antarctic Ice Sheet (AIS) mass balance through enhanced snowfall (Turner et
49 al., 2019; Wille et al., 2021; MacLennan et al., 2022), but they can also induce surface melt and promote ice-shelf instability
50 when transporting warm, moist air masses inland (Gorodetskaya et al., 2014; Adusumilli et al., 2021; Wille et al., 2019; Wille
51 et al., 2022). Given their dual role, robust detection of ARs is essential for quantifying their frequency and impacts.

52

53 Many AR detection tools (ARDTs) have been developed for different purposes and regions (Collow et al., 2022), but only a
54 few are tailored to polar environments (Wille et al., 2021; Gorodetskaya et al., 2014; Mattingly et al., 2018; Wille et al., 2025).
55 At the global scale, the most widely used scheme remains that of Guan and Waliser (2015). It employs seasonally and spatially
56 varying vertically integrated water vapor transport (IVT) thresholds (85th percentile), which provide broad applicability and
57 robust intercomparison across reanalyses (Collow et al., 2022). The method also includes a minimum feature length of 2000
58 km (Zhu and Newell, 1998) and additional directional and coherence constraints, requiring a minimum poleward IVT
59 component and a coherent IVT direction. However, the Guan and Waliser framework shows limited skill over Antarctica, as
60 its lower IVT percentile threshold tends to identify extensive zonal moisture bands that circulate around the ice sheet without
61 significant inland penetration.



62

63 For Antarctica, the most widely used polar-specific ARDT is that of Wille et al. (2021), which includes two variants of the
64 same method applied to different input variables: the meridional component of IVT (vIVT, hereafter Wille vIVT) and vertically
65 integrated water vapor (IWV, hereafter Wille IWV). Among these, the vIVT-based version is the most commonly used. It
66 applies a monthly, locally defined 98th-percentile threshold on vIVT, combined with a 20° meridional extent criterion, to
67 identify the strongest southward moisture intrusions linking the lower latitudes to the Antarctic continent. This design is
68 physically consistent with the dynamics of extreme Antarctic precipitation, as intense snowfall events are generally associated
69 with above-average IVT directed southward and approximately perpendicular to the coast (Wille et al., 2021). Consequently,
70 the Wille vIVT scheme effectively isolates the ARs that have been linked to intense precipitation (Wille et al., 2021; Maclennan
71 et al., 2022), surface melt (Wille et al., 2019, Gorodetskaya et al., 2023), firn depletion, large iceberg calving events, and ice-
72 shelf destabilization (Wille et al., 2022). Thus, this ARDT has become the reference framework for polar AR studies (Wille et
73 al., 2025).

74

75 However, the Wille et al. (2021) framework, while robust, does not capture the full range of intense moisture transport features
76 relevant to Antarctica. While weaker or more diffuse intrusions are rightly excluded by design, some long, narrow, and intense
77 filaments of water vapor transport, dynamically consistent with the physical definition of ARs (American Meteorological
78 Society, 2022), remain undetected. This underdetection arises from methodological constraints related to the orientation,
79 coherence, and geometric requirements of the detection scheme.

80

81 First, the use of vIVT in the Wille vIVT scheme introduces a discontinuity at the South Pole. When an AR crosses the pole,
82 the sign of vIVT reverses from poleward to equatorward, preventing its identification. This discontinuity also breaks the
83 continuity of the feature's axis, preventing it from satisfying the minimum length criterion (20° meridional extent) at the
84 highest latitudes. This issue does not affect the Wille IWV scheme, which does not consider the meridional wind; however,
85 Wille et al. (2021) restricted their detection domain to 85° S (Fig. 1b) to avoid this singularity, in both vIVT and IWV schemes,
86 to maintain consistency of AR climatologies between both algorithms. While this boundary had little impact on coastal AR
87 landfalls and when tracking their progression inland, it introduces a progressive detection bias toward lower latitudes, up to
88 around 65° S, as a result of the 20° meridional extent requirement.

89

90 Second, focusing on “moisture transport axes,” a term introduced to unify ARs, tropical moisture exports, and warm moist
91 intrusions; Spensberger et al. (2025) note that one third of those axes exhibit an equatorward component. This behavior likely
92 reflects synoptic-scale processes such as frontal occlusion and the curvature of moisture pathways within mature cyclones, as
93 well as the modulation of moisture transport by quasi-stationary large-scale circulation features and topographic forcing. As
94 these systems move poleward and their associated ARs approach the Antarctic coast, they interact with the prevailing near-
95 surface easterlies and the steep topography of the ice sheet margin. These interactions often cause the moisture plumes to curve



96 or tilt at landfall, deviating from a purely meridional orientation. Approximately 20% of “moisture transport axes” south of
97 70° S display such equatorward curvature (Spensberger et al., 2025). This behavior is particularly common in the Ross Sea
98 and Weddell Sea regions (see Fig. 1a for geographic regions referenced in this study), where synoptic and orographic effects
99 jointly steer moisture fluxes away from the meridional direction. In these cases, vIVT decreases and reverses sign as the AR
100 curves equatorward, leading to a loss of detection at and beyond the inflection point. Although this specific limitation does not
101 affect the Wille IWV scheme, it remains constrained by the 20° meridional extent criterion, which also excludes long, curved,
102 or overturning ARs that are dynamically consistent with AR characteristics but have limited meridional span due to their
103 complex geometry. This limitation is not unique to the Wille et al. (2021) framework, as global AR detection schemes such as
104 Guan and Waliser (2015) also omit such events because their directional-coherence criteria preclude the detection of curved
105 or horseshoe-shaped ARs.

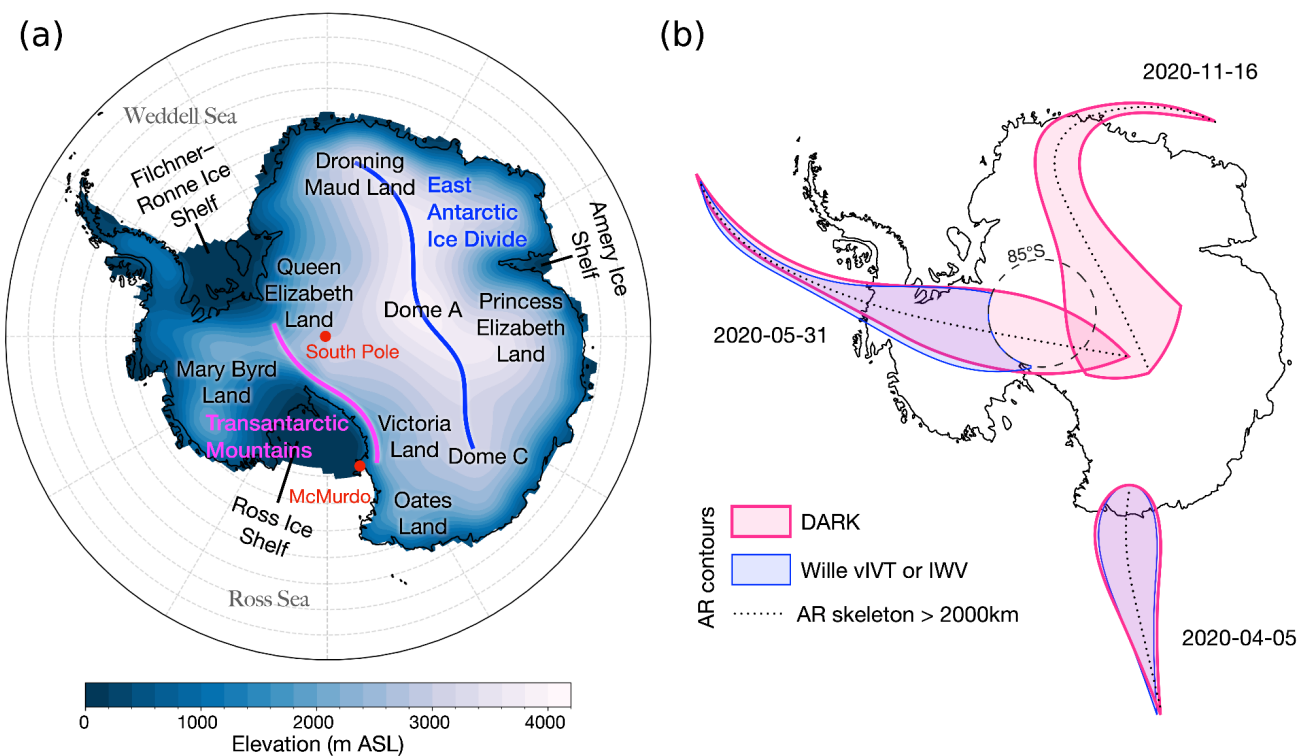
106

107 Another limitation of existing detection approaches concerns the evolution of ARs after they reach the Antarctic continent.
108 As they make landfall, they often diverge and lose their narrow filamentary geometry due to condensation, latent heat release,
109 and the spreading of moisture fluxes within occluding or decaying frontal systems (Dacre and Clark, 2025). Although this
110 morphological transition causes them to fall outside the geometric criteria of standard AR detection methods, these features
111 frequently remain highly moisture-laden and continue to drive precipitation, cloud formation, and surface melt inland. To
112 capture the continuation of AR influence, identifying and tracking such post-landfall remnants would be relevant but has not
113 yet been proposed. This would allow the monitoring of structures representing the inland evolution of decaying but still active
114 AR-provided moisture remnants. Accounting for these structures would be essential for quantifying the sustained hydrological
115 and thermodynamic effects of ARs on the Antarctic surface mass balance, while extending the study of the Antarctic AR life
116 cycle to its terminus (Wille et al., 2024).

117 To address these limitations, we develop a new Antarctic ARDT called DARK (Detecting ARs using their Kurvature), that
118 builds upon the intensity-based framework of Wille et al. (2021) while removing directional constraints that limit the
119 identification of curved or equatorward-turning ARs (like the AR making landfall on 2020-11-16, in Dronning Maud Land,
120 Fig. 1b). The method applies a 98th-percentile threshold on total integrated vapor transport (IVT), computed using a 15-day
121 rolling window to capture temporal variability and regional seasonality. Features smaller than 20,000 km² are removed prior
122 to classification. ARs are then defined as contiguous structures exceeding the IVT threshold with a total length of at least 2000
123 km, approximately equivalent to the 20° meridional extent criterion of Wille et al. (2021) (Fig. 1b), but regardless of their
124 orientation or directional coherence. In addition, we introduce an add-on to identify and track post-landfall moisture remnants
125 with IVT above the local 98th-percentile, which evolve from previously detected ARs but no longer meet the geometric length
126 criterion, hereafter referred to as AR-children. This study aims to illustrate that our framework provides a more complete and
127 physically consistent view of AR-driven moisture transport and its influence on Antarctic precipitation and near-surface
128 temperature variability, with implications for surface melt and ice-shelf stability.



129 We apply this framework to a multi-decadal ERA5 reanalysis (1979–2023) to produce the first comprehensive assessment of
130 Antarctic ARs that explicitly includes curved ARs (hereafter DARK ARs) and their post-landfall AR-children. The analysis
131 quantifies their contribution to Antarctic precipitation, as well as to precipitation, temperature, and compound anomalies and
132 extremes. It further characterizes the magnitude and orientation of IVT and presents representative case studies illustrating
133 their synoptic evolution. This framework aims to fill key observational and methodological gaps left by existing ARDTs,
134 providing a more comprehensive representation of Antarctic ARs and their impacts on the AIS.



135

136 **Figure 1.** (a) Map of the Antarctic Ice Sheet (AIS) showing surface elevation (m a.s.l.) and key geographic regions discussed
137 in the text. (b) Conceptual schematic illustrating detection differences between the DARK and Wille AR frameworks during
138 three representative landfall events.

139 **2 Data and methodology**

140 **2.1 Data**

141 We use the ERA5 reanalysis produced by the European Centre for Medium-Range Weather Forecasts (ECMWF; Hersbach et
142 al., 2020) for the period 1979–2023, at a horizontal resolution of $0.25^\circ \times 0.25^\circ$. Atmospheric rivers are detected at 6-hourly



143 intervals using the zonal (uIVT) and meridional (vIVT) components of integrated vapor transport (IVT). Diagnostic variables,
144 including wind and geopotential height at 500 hPa, are analyzed at the same 6-hourly timestep.
145 Surface diagnostics are evaluated at daily resolution: total precipitation is aggregated to daily sums, and 2 m air temperature
146 is used to derive daily maximum values.

147 For intercomparison, the Wille et al. (2021) Antarctic AR detection schemes based on integrated water vapor (IWV) and
148 meridional IVT (vIVT) were recomputed at 6-hourly intervals. To ensure spatial consistency with the new DARK framework,
149 both Wille schemes were extended northward to 15° S while retaining their original southern boundary at 85° S. This
150 adjustment provides uniform temporal and spatial coverage across methods, enabling a direct comparison of AR frequency,
151 geometry, and associated surface impacts over the 1979–2023 period.

152

153 2.2 DARK AR Detection Algorithm

154

155 At each 6-hourly time step, the DARK framework is applied over the 15° S–90° S domain. The magnitude of IVT is computed
156 from its zonal and meridional components as

157
$$IVT = \sqrt{uIVT^2 + vIVT^2} \quad (1)$$

158 where $uIVT$ and $vIVT$ are the zonal and meridional components of IVT from ERA5.

159 A rolling 15-day 98th-percentile threshold of IVT is calculated for each grid point and day of year using all available years
160 (1979–2023). Grid cells exceeding this threshold are identified at each 6-hourly time step and grouped into contiguous features
161 using a connectivity criterion that links all directly adjacent or diagonally touching cells. Objects smaller than 20,000 km² are
162 removed before centerline computation to avoid processing small, isolated exceedances that are not representative of large-
163 scale moisture transport and for which centerline estimation is computationally expensive and prone to numerical error.

164

165 The remaining features are reduced to a one pixel wide skeleton using a morphological thinning algorithm. This skeleton is
166 then converted into a graph representation from which all endpoint-to-endpoint paths are extracted. The longest and most
167 directionally consistent path, determined using principal component analysis, is selected as the primary centerline. The path is
168 extended to the object's edge, smoothed using a B-spline interpolation, and resampled to 200 evenly spaced points. The total
169 AR length is finally computed as the geodesic distance along this smoothed centerline, while accounting for longitudinal
170 wrapping. An object is classified as an AR if its total centerline length is equal to or greater than 2000 km, consistent with the
171 typical length scale used in established AR detection frameworks (e.g., Guan and Waliser, 2015; Wille et al., 2021; Skinner et
172 al., 2020; Gorodetskaya et al., 2014). This procedure yields a binary AR mask indicating the presence or absence of an AR at
173 each grid point and timestep.



174

175 **2.3 Optional AR-children add-on**

176

177 The AR-children add-on is an optional extension of the main detection algorithm. It builds upon the AR catalog described
178 above to identify post-landfall moisture structures that remain intense after the parent AR loses spatial coherence. Accordingly,
179 two catalogs are provided: one including only DARK ARs and another combining DARK ARs with their AR-children, with
180 accompanying binary and classification variables (see Data Availability). At each time step, regions where IVT exceeds the
181 98th-percentile threshold are labeled as contiguous features using a connectivity criterion that links all directly adjacent or
182 diagonally touching grid cells. Temporal continuity is established through spatial overlap between consecutive time steps,
183 ensuring consistent tracking of moisture structures while maintaining computational efficiency. A feature is classified as an
184 AR-child when it spatially overlaps with a parent AR of the previous timestep and subsequently detaches from it while being
185 in contact with, or located over, the Antarctic continent. A minimum area of 20,000 km² is imposed to exclude small structures.
186 This approach ensures both physical and temporal consistency while remaining computationally efficient for multi-decadal,
187 hemispheric reanalysis datasets.

188

189 **2.4 Attribution of events to ARs**

190

191 To attribute surface impacts to ARs (or AR-children), we identify precipitation and temperature events temporally associated
192 with AR occurrence. Because AR-related precipitation and temperature anomalies can persist beyond the period when a given
193 grid cell is directly affected by an AR, the attribution window is extended to include adjacent days, depending on the variable.

194

195 For precipitation, AR-related events are defined as those occurring on the day of AR landfall (D₀) and the following day (D₊₁),
196 following Wille et al. (2021) and Maclennan et al. (2022). We use here a daily timescale for computing efficiency and to avoid
197 multiple detections of single extreme events due to serial correlation at sub-daily timescales. This extension accounts for
198 residual precipitation that continues after the main AR plume loses coherence or moves inland.

199

200 For temperature, AR-related events are considered on the day before (D₋₁), the day of (D₀), and the day after (D₊₁) AR landfall.
201 This accounts for both preconditioning (e.g., warm advection ahead of the AR) and lagged warming due to persistent cloud
202 cover, latent heat release, or surface melt following AR passage.

203

204 For precipitation, daily totals are compared to the mean daily climatology for each calendar day (1979–2023), while for 2 m
205 air temperature, daily maxima are compared with the corresponding daily-maximum climatology. In both cases, the anomaly
represents the deviation from the daily mean climatological value at each grid point.



206 Extreme events are defined as days when these anomalies exceed the 99th percentile of their respective daily anomaly
207 distributions, computed independently at each grid point. Compound events, defined as the co-occurrence of extreme
208 precipitation and temperature anomalies, are identified when an extreme precipitation day coincides with or occurs within ± 1
209 day of an extreme temperature anomaly. This temporal window ensures that temporally overlapping or closely spaced extremes
210 are captured within a single compound-event framework. This approach allows both direct and short-lagged compound
211 extremes associated with ARs to be included in the analysis.

212 2.5 Risk Ratio

213 Because extending the attribution window naturally increases the number of AR-associated events, we quantify their statistical
214 relevance using risk ratios (RR). This ensures that higher counts reflect genuine physical associations rather than the effect of
215 broader temporal inclusion. RR are computed as the ratio between the probability of an extreme event during AR conditions
216 (Eq. 2) and the probability during non-AR conditions (Eq. 3).

217 For each grid point, the conditional probabilities are defined as:

$$218 P(E | AR) = \frac{N_{E,AR}}{N_{AR}} \quad (2)$$

$$219 P(E | \neg AR) = \frac{N_{E,\neg AR}}{N_{\neg AR}} \quad (3)$$

220 where $N_{E,AR}$ is the number of days with both an AR and an extreme event (considering the temporal extension defined in Sect.
221 2.5), N_{AR} is the total number of AR days (including the temporal extensions defined in Sect. 2.5), $N_{E,\neg AR}$ is the number of
222 extreme events without an AR, and $N_{\neg AR}$ the number of non-AR days.
223 RR is then expressed as:

$$224 RR = \frac{P(E|AR)}{P(E|\neg AR)} \quad (4)$$

225 Values of $RR > 1$ indicate that extreme events are more likely under AR conditions. For example, a value of $RR = 2$ implies
226 that extreme events are twice as likely to occur during AR conditions compared to non-AR conditions. This metric accounts
227 for the frequency of AR occurrence, ensuring that results reflect the relative enhancement of extremes rather than the
228 prevalence of ARs themselves.

230 2.6 Statistical significance

231 Differences in AR occurrence between schemes were evaluated using a two sample test of equality of proportions at each grid
232 point. For the share of precipitation attributable to ARs, as well as for precipitation intensity (the ratio of AR-related
233 precipitation to AR occurrence), extreme precipitation, temperature, and compound events, significance was assessed using
234 the same bootstrap framework: AR dates (including their variable-dependent temporal extensions) were kept fixed, while entire
235



236 precipitation or temperature years were permuted without replacement, preserving their autocorrelation and seasonality but
237 breaking their co-occurrence with ARs. The observed AR-associated fraction (or the difference between detection schemes)
238 was compared against 1000 bootstrap realizations, and values were considered significant when they lay outside the
239 corresponding 95 % bootstrap confidence interval.

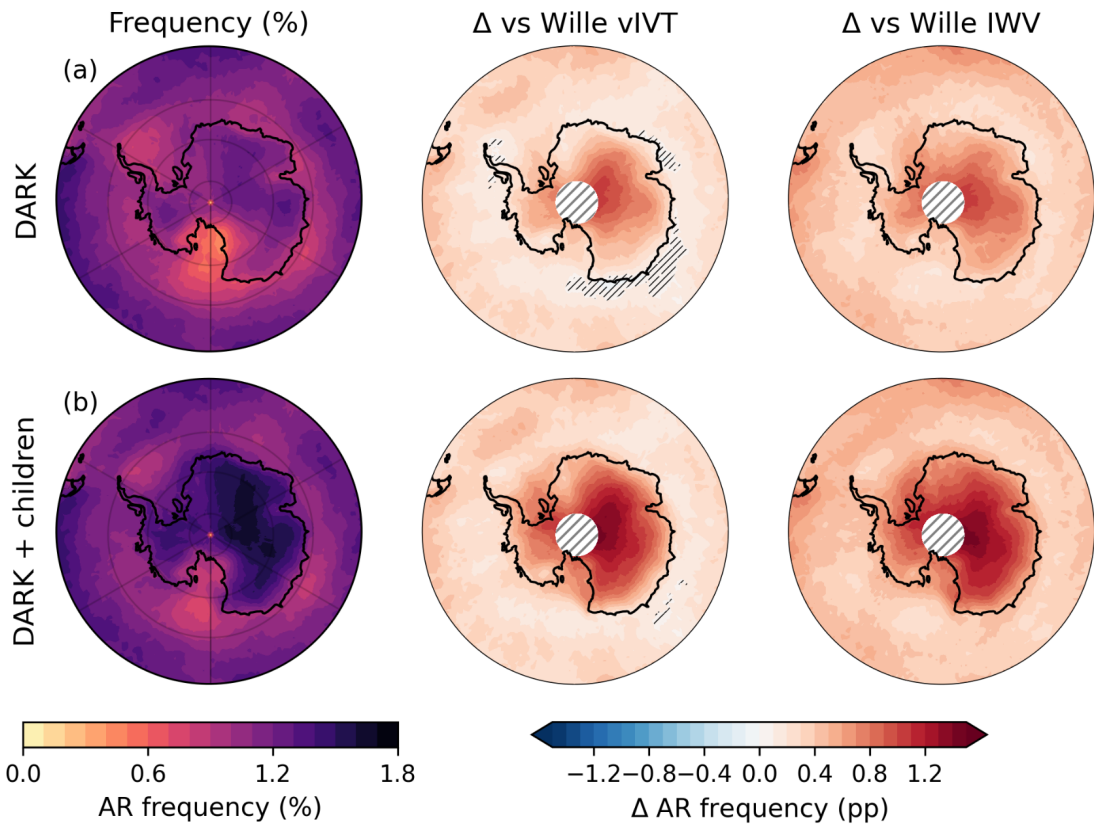
240

241 The statistical significance of the RRs was assessed following the log-normal approximation method of Katz et al. (1978). To
242 handle zero count cases, we applied the Haldane–Anscombe correction by adding 0.5 to both co-occurrence counts and 1 to
243 the total-event denominators. A 95 % confidence interval was computed on the log-transformed RR and then exponentiated
244 back to the RR scale. Grid cells were considered significant when the confidence interval excluded 1; otherwise, they were
245 masked as non-significant.

246 **3 Results**

247 **3.1 Frequency of DARK ARs and AR-children**

248 DARK ARs exhibit their highest occurrence within the midlatitude storm-track regions (Fig. 2a) (Chang et al., 2002; Wirth et
249 al., 2018), with maxima during austral winter (see Fig. S1). The lowest frequencies occur over the Ross Sea sector, where the
250 minimum is most pronounced in winter. The spatial distribution closely matches that of Wille vIVT and Wille IWV schemes,
251 although DARK ARs yields higher overall frequencies, particularly over the AIS. Over South of the East Antarctic Ice Divide
252 (EAID, Fig. 1a), occurrence is up to 1.2 percentage points (pp) higher than in Wille vIVT and IWV, while along the East
253 Antarctic coast the difference remains small (≈ 0.3 pp), indicating that the total frequency of AR landfalls along the Antarctic
254 coastline remains roughly unchanged between the Wille and DARK schemes. By construction, AR-children occur exclusively
255 over the continent and its coastal margins, with mean frequencies up to 0.3 % along the coast and local maxima of 0.6 % near
256 McMurdo and farther inland over the plateau (Fig. S2a), bringing the total frequency of DARK ARs and their AR-children at
257 1.5 % across most of the AIS (Fig. 2b).



258

259 **Figure 2.** Frequency of DARK atmospheric rivers (ARs) (a) and DARK ARs and their children (b). Left panels: AR occurrence
260 (%) Middle and right panels: differences from the Wille vIVT and Wille IWV schemes (percentage points, pp). Hatched white
261 areas south of 85° S mark regions without data in the Wille schemes, hatches elsewhere cover non-significant regions (Sect.
262 2.6).
263

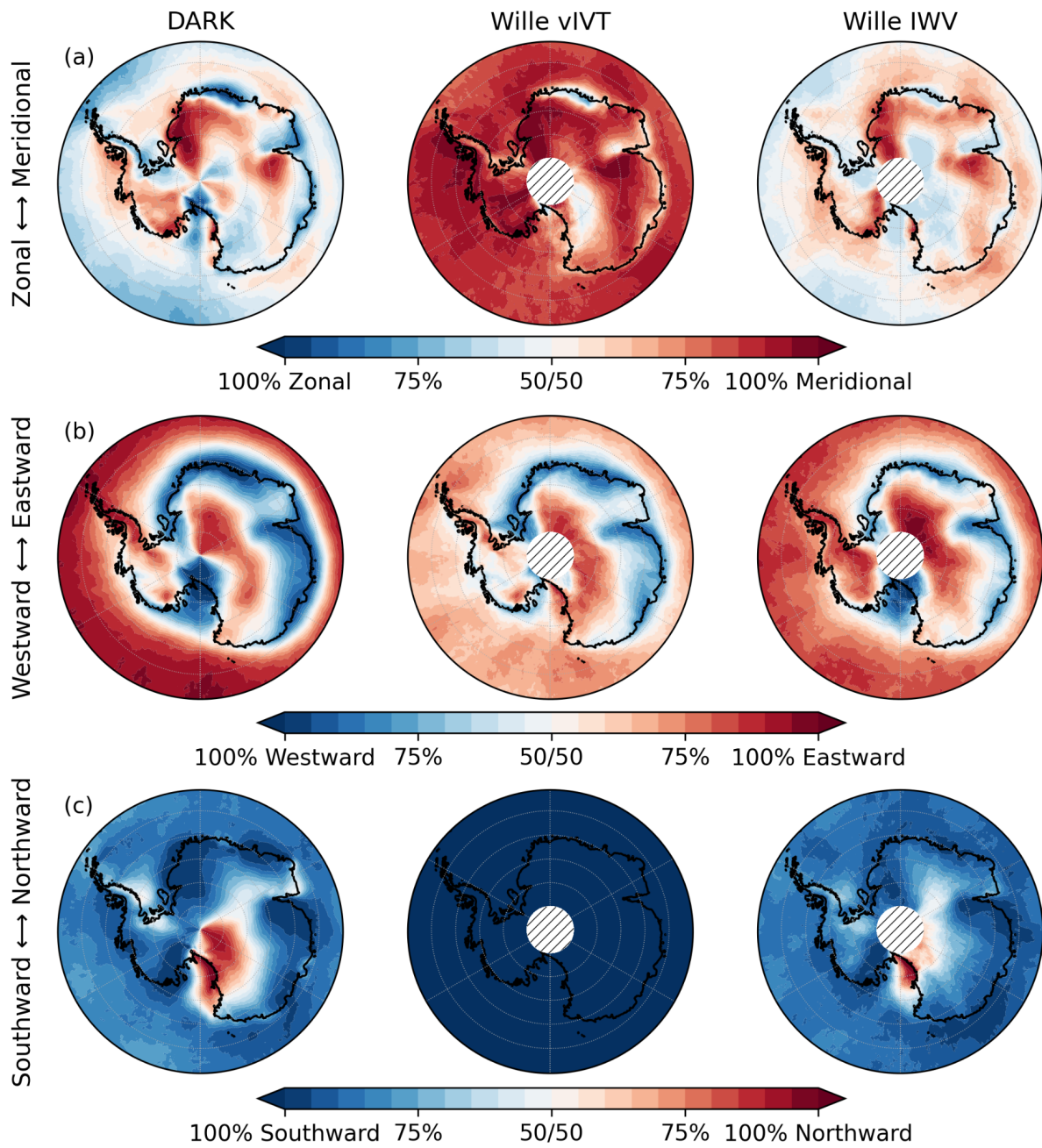
264

3.2 Direction and orientation of DARK ARs

265 DARK ARs exhibit a much wider range of orientations than either Wille schemes while still reproducing well the dominant
266 large-scale IVT orientation patterns (zonal versus meridional, and eastward versus westward) captured by Wille IWV (Fig. 3a,
267 c). A majority of Wille vIVT ARs are also detected by DARK, with 64 % agreement over the Southern Ocean and about 61
268 % on average across the AIS (Fig. S3a). The co-detection is strongest where DARK ARs exhibit predominantly meridional,
269 southward orientations, such as over southern Dronning Maud Land, Coats Land, and along the northern flank of the East
270 Antarctic Ice Divide. However, a substantial fraction of ARs detected by DARK are not captured by Wille vIVT: across the
271 Antarctic Ice Sheet, roughly 67 % of DARK ARs are exclusive to the new detection framework (Fig. S3b). These additional



272 detections are particularly frequent from the Ross Ice Shelf to Dome A along the southern flank of the East Antarctic Ice
273 Divide. In these regions, DARK ARs are mainly northward (Fig. 3c; and eastward, due to the influence of the East Antarctic
274 topography and the Coriolis deflection of the pressure-driven circulation) oriented, which is incompatible with Wille's strict
275 requirement of southward vIVT. Elsewhere across the continent, all three schemes, DARK, Wille vIVT, and Wille IWV, show
276 predominantly southward-oriented ARs, confirming that most intense moisture transport toward Antarctica occurs in a
277 poleward direction. Wille vIVT ARs that do occur there generally correspond to relatively strong meridional, but weak total
278 IVT, since the percentile-based threshold can be met even under low IVT. In contrast, DARK detects ARs in these sectors
279 because they exceed the 98th-percentile threshold in total IVT, capturing dynamically stronger but more geometrically
280 complex structures. Compared with Wille IWV, DARK shows a more homogeneous agreement across the AIS, with up to 90
281 % co-detection in Dronning Maud Land (Fig. S3a). This higher overlap reflects the greater directional flexibility of Wille
282 IWV, which can capture zonal or northward ARs (Fig. 3a,c), including those turning over the Ross and Amery Ice Shelves
283 and along the East Antarctic coastline. However, Wille IWV remains limited by its 20° meridional extent criterion, which
284 disfavors fully zonal filaments. Moreover, because IWV represents static moisture rather than dynamic transport, it detects
285 only about 50 % of DARK ARs in localized regions such as the Dronning Maud Land coast (Fig. S3b). These undetected cases
286 typically contain high humidity but insufficient wind to produce large IVT values, preventing them from meeting the DARK
287 threshold. Overall, Wille vIVT and IWV ARs only partially overlap with DARK detections. A majority of Wille (vIVT or
288 IWV) ARs are identified by DARK, but many DARK ARs are not detected by Wille ARDTs. This asymmetry highlights that
289 while the methods share a common physical basis, DARK extends beyond Wille's directional and geometric constraints,
290 capturing a more dynamically coherent and diverse range of AR geometries, including curved, zonal, and poleward-turning
291 filaments that were missed by previous frameworks.



292

293 **Figure 3.** Fraction of AR time characterized by (a) zonal vs. meridional dominant IVT components (uIVT vs. vIVT), (b)
294 westward vs. eastward, and (c) southward vs. northward IVT anomalies relative to climatology, for DARK (left), Wille vIVT
295 (middle), and Wille IWV (right). Hatched white areas south of 85° S mark regions without data in the Wille schemes.

296



297 **3.2 Contribution of ARs to Antarctic precipitation**

298

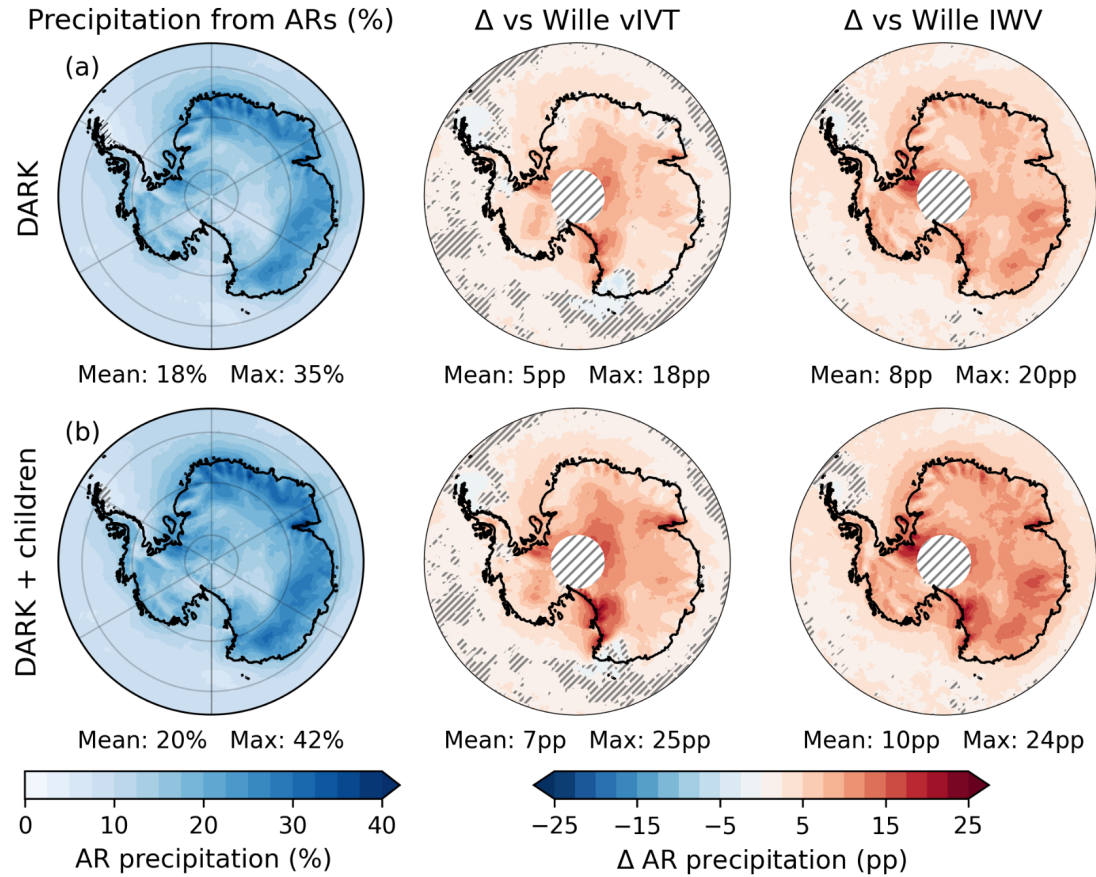
299 DARK ARs account for an average of 18 % of total AIS precipitation, reaching up to 35 % in some regions (Fig. 4a). Only
300 along the relatively straight, zonally oriented sectors of the East Antarctic coastline, their contribution is comparable to that of
301 Wille vIVT ARs. In contrast, in areas where the coastline geometry departs from this alignment, particularly within the major
302 embayments such as the Ross, Ronne–Filchner, and Amery Ice Shelves, DARK ARs contribute to substantially more
303 precipitation, with enhanced signals extending inland over the catchments located south of the EAID. The only region where
304 DARK ARs contribute to less precipitation than Wille vIVT ARs is Oates Land.

305 On average, DARK ARs deliver 5 (8) pp more precipitation than Wille vIVT (Wille IWV), with local increases up to 18 (20)
306 pp in the interior, notably near the South Pole and the Transantarctic Mountains. Even when both Wille schemes are combined,
307 DARK ARs still produce 2 pp more precipitation on average, with local differences reaching up to 15 pp (Fig. S4). AR-children
308 contribute little on average (Fig. 4b) but represent a significant additional source within these embayments, most notably over
309 the Amery Ice Shelf and Victoria Land, where they account for more than 8 % of total AIS precipitation (Fig. S2b).

310 In this analysis, precipitation occurring on the day of AR landfall (D_0) and the following day (D_{+1}) is attributed to ARs
311 throughout this study (Sect. 2.4), and to ARs and their children when using the DARK+children framework, consistent with
312 common practice (Wille et al., 2021; Maclennan et al., 2022). When AR-children are included, however, a comparable AIS-
313 averaged share of precipitation is obtained (Fig. S5) even when considering precipitation associated with DARK ARs and their
314 children on the day of landfall alone (D_0), compared to attributing precipitation to DARK ARs without including AR-children
315 over both the day of landfall (D_0) and the following day (D_{+1}). This reflects not a temporal substitution, but a spatial refinement:
316 AR-children explicitly capture the inland propagation and dissipation of moisture that, in previous approaches, was only
317 approximated by extending the temporal attribution window beyond landfall. Their inclusion therefore provides a more
318 physically consistent representation of post-landfall hydrological impacts.

319

320



321

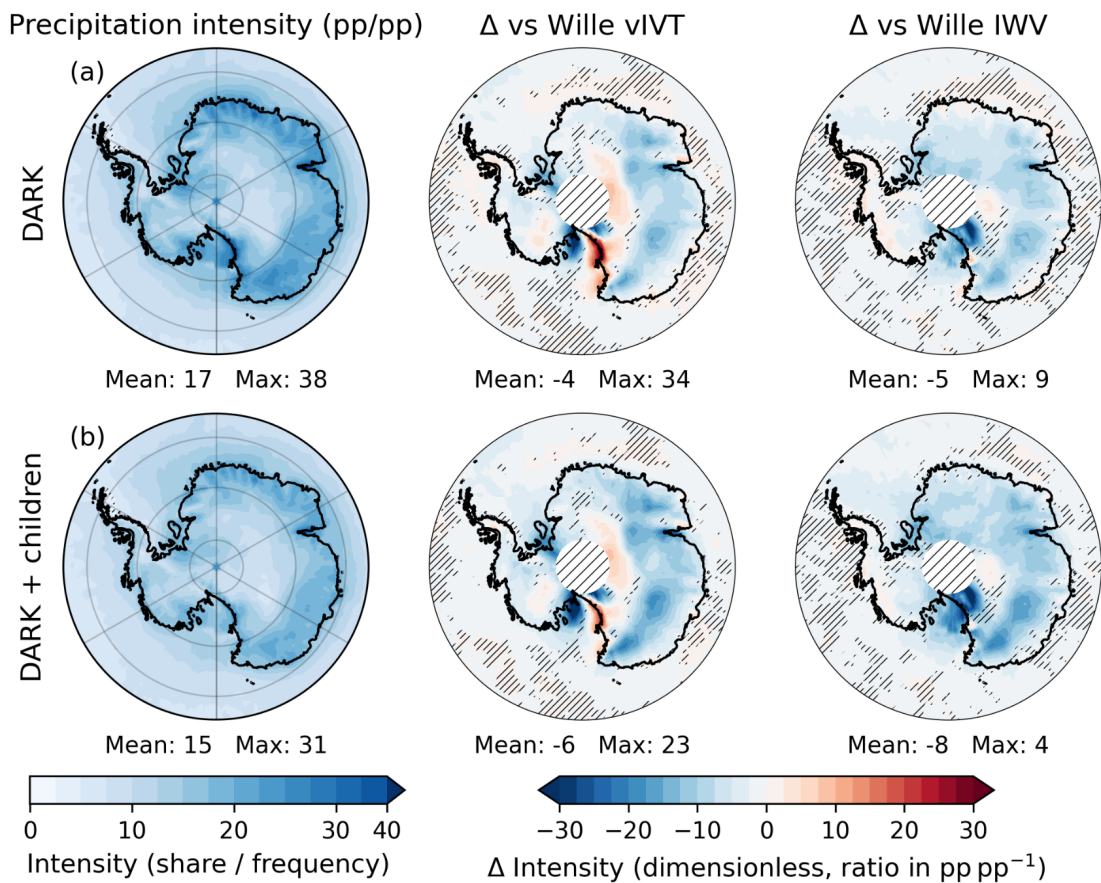
322 **Figure 4.** Share of total precipitation attributed (Sect. 2.4) to (a) DARK ARs and (b) DARK ARs and their children. Left
323 panels: percentage of precipitation from ARs. Middle and right panels: differences from the Wille vIVT and Wille IWV
324 schemes (pp). Antarctic land-only (inside-coastline) mean and maximum values are reported below each panel. Hatched white
325 areas south of 85° S mark regions without data in the Wille schemes, hatches elsewhere cover non-significant regions (Sect.
326 2.6).

327

328 While DARK ARs contribute more to precipitation than either Wille scheme across most of the AIS, this increase primarily
329 reflects their higher occurrence frequency rather than higher precipitation per event (Fig. 5a). When normalized by AR
330 occurrence, that is, expressed as the ratio of AR-related precipitation (%) to AR occurrence (%), the mean precipitation
331 intensity (pp pp⁻¹, dimensionless) associated with DARK ARs is slightly lower overall than in both Wille schemes (around -
332 5). Relative to Wille IWV, precipitation intensity is lower across the AIS in a broadly uniform pattern. However, relative to
333 Wille vIVT, differences are more heterogeneous: intensity is reduced over most of the AIS but locally enhanced over the
334 Amery Ice Shelf and south of the EAID, peaking along the Ross sector of the Transantarctic Mountains (up to 34). When



335 DARK ARs and their associated children are considered together, the overall AR intensity further decreases, although they
336 remain more intense than Wille ARs in the latter regions (Fig. 5b).



337

338 **Figure 5.** Normalized AR precipitation intensity, defined as the ratio between the percentage of precipitation from ARs (Fig.
339 2) and AR frequency (Fig. 2, dimensionless), for (a) DARK ARs and (b) DARK ARs and their children. Middle and right
340 panels: differences from the Wille vIVT and Wille IWV schemes (pp). Antarctic land-only mean and maximum values are
341 reported below each panel. Hatched white areas south of 85° S mark regions without data in the Wille schemes.

342 3.3 Contribution to extreme events

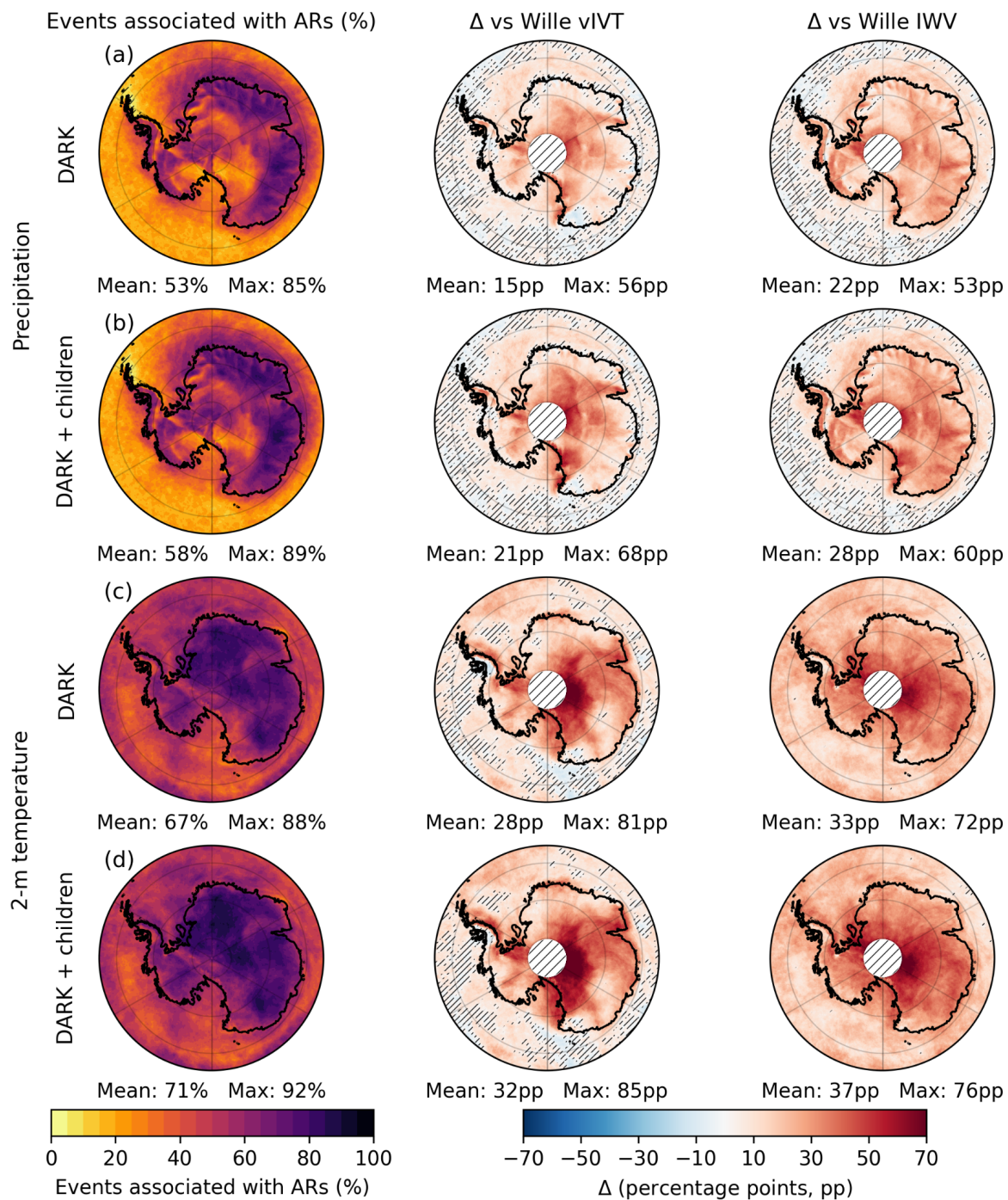
343 DARK ARs are associated with 53 % of extreme (Sect. 2.4) precipitation days on average (Fig. 6a), with local values reaching
344 up to 85 % inland of the East Antarctic coast and decreasing toward Dome C. Although the mean precipitation per AR event
345 is lower (Sect. 3.2), the DARK scheme captures a substantially larger proportion of the most intense precipitation anomalies



346 than either Wille scheme. Compared to Wille vIVT, the association fraction is higher by 15 pp on average and locally by up
347 to 56 pp south of the EAID, with only a few small areas showing slightly weaker associations, the largest being Oates Land.
348 Relative to Wille IWV, the increase is more spatially homogeneous, with the largest differences following topography,
349 particularly over Queen Elizabeth Land. This pattern indicates that DARK, like Wille vIVT, better represents topographically
350 induced precipitation linked to moisture transport rather than static humidity. Including AR-children increases the mean
351 association by only about 5 pp (Fig. 6a,b), but they remain locally significant, forming broad hotspots over the Amery Ice
352 Shelf and across Victoria Land, where they account for more than 15 %, and locally up to 20 %, of extreme precipitation days
353 (Fig. S6). These regions represent the strongest and most spatially extensive contributions of AR-children, while more
354 localized contributions also occur south of the EAID, where post-landfall moisture remnants sustain intense precipitation after
355 the parent AR dissipates.

356 DARK ARs are associated with 67 % of extreme daily maximum temperature events on average (Sect. 2.4; Fig. 6c), with local
357 values exceeding 80 % near Dome C and over Dronning Maud Land. Compared to the Wille schemes, DARK increases the
358 association fraction by more than 28 pp on average. The gain is spatially uniform relative to Wille IWV and more spatially
359 contrasted compared to Wille vIVT, with the largest improvements south of the EAID. Including AR-children further raises
360 the mean association to approximately 71 % (Fig. 6d), primarily through a uniform increase of about 4 pp across most of the
361 AIS. In several regions, this leads to association fractions exceeding 90 % locally, while the largest increases occur over
362 Victoria Land and the Ross Ice Shelf–McMurdo area, where AR-children contribute up to 20 pp of additional extreme
363 temperature events. This reflects the persistence of warm, moist air masses following AR landfall (Fig. S6).

364 Compound (precipitation and 2 m air temperature) extremes (Sect. 2.4) occur widely across Antarctica but are absent leeward
365 of the Antarctic Peninsula, where strong foehn winds produce warm but dry conditions (Fig. S7). DARK ARs are associated
366 with approximately 78 % of compound extremes on average (Fig. 7a) and with nearly 100 % across broad sectors of East
367 Antarctica. DARK identifies substantially more inland events than Wille vIVT, which captures many compound events along
368 the coast but misses large interior regions south of the EAID, from southern Dronning Maud Land to Victoria Land and around
369 the Amery Ice Shelf. Including AR-children increases the mean association modestly (by about 3 pp) but introduces a distinct
370 new hotspot over Victoria Land (Fig. 7b), where AR-children contribute to more than 20 pp of additional compound extremes
371 (Fig. S6). Notably, Victoria Land is also one of the two main regions of frequent compound events across the continent,
372 although such events remain rare overall (fewer than 0.5 % of days: Fig. S7).



373

374

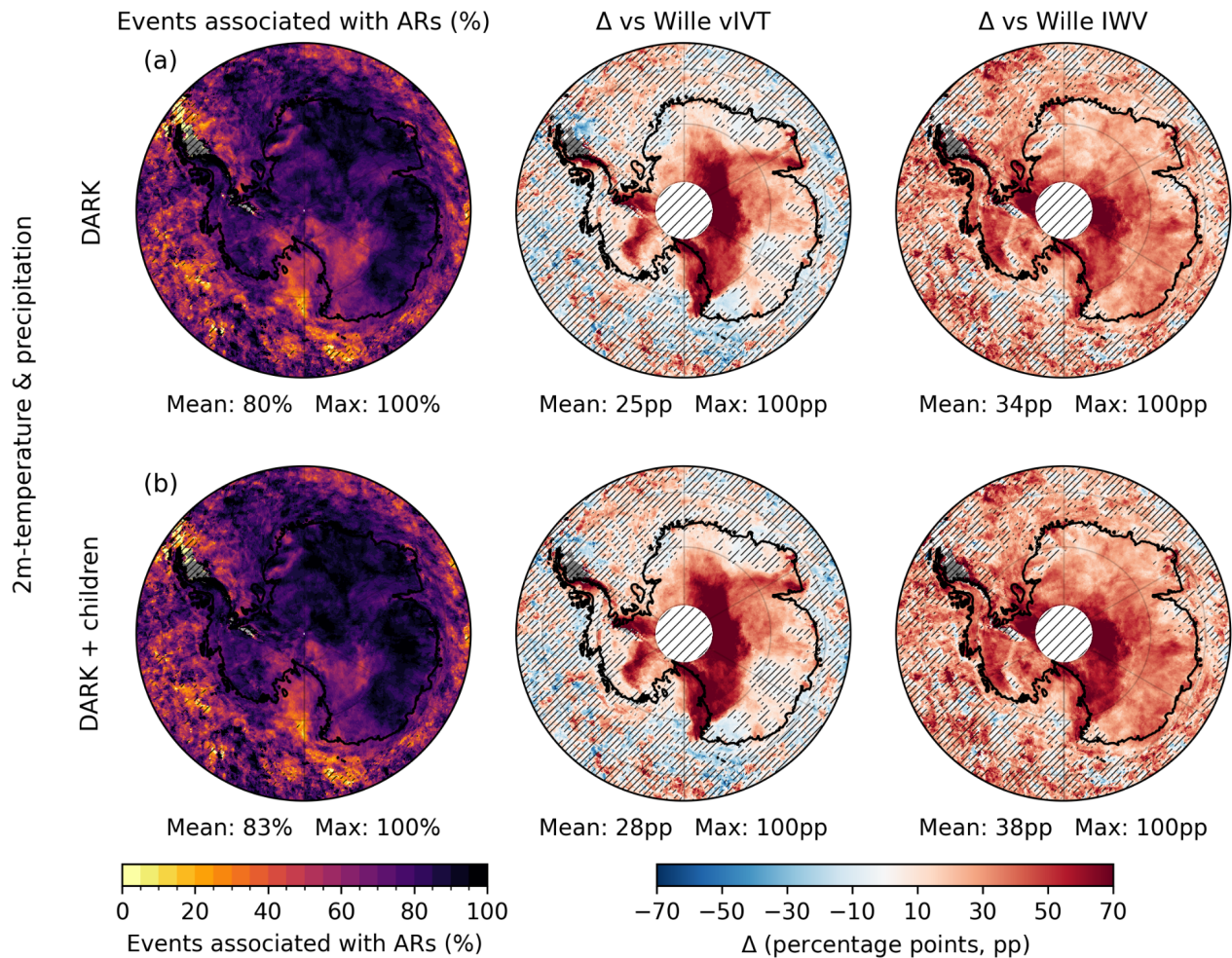
375

376

Figure 6. Fraction of 99th-percentile anomaly days attributed (Sect. 2.4) to DARK ARs for precipitation (rows a–b) and 2 m temperature (rows c–d). Within each variable, the first row shows DARK ARs and the second row shows DARK ARs and their children. Columns show (left to right) the absolute fraction of extremes and the differences relative to the Wille vIVT

377 and Wille IWV schemes (percentage points, pp). Antarctic land-only mean and maximum values are reported below each
378 panel. Hatched white areas south of 85° S mark regions without data in the Wille schemes; hatched overlays indicate non-
379 significant values; gray shading indicates grid cells with no detected extremes.

380

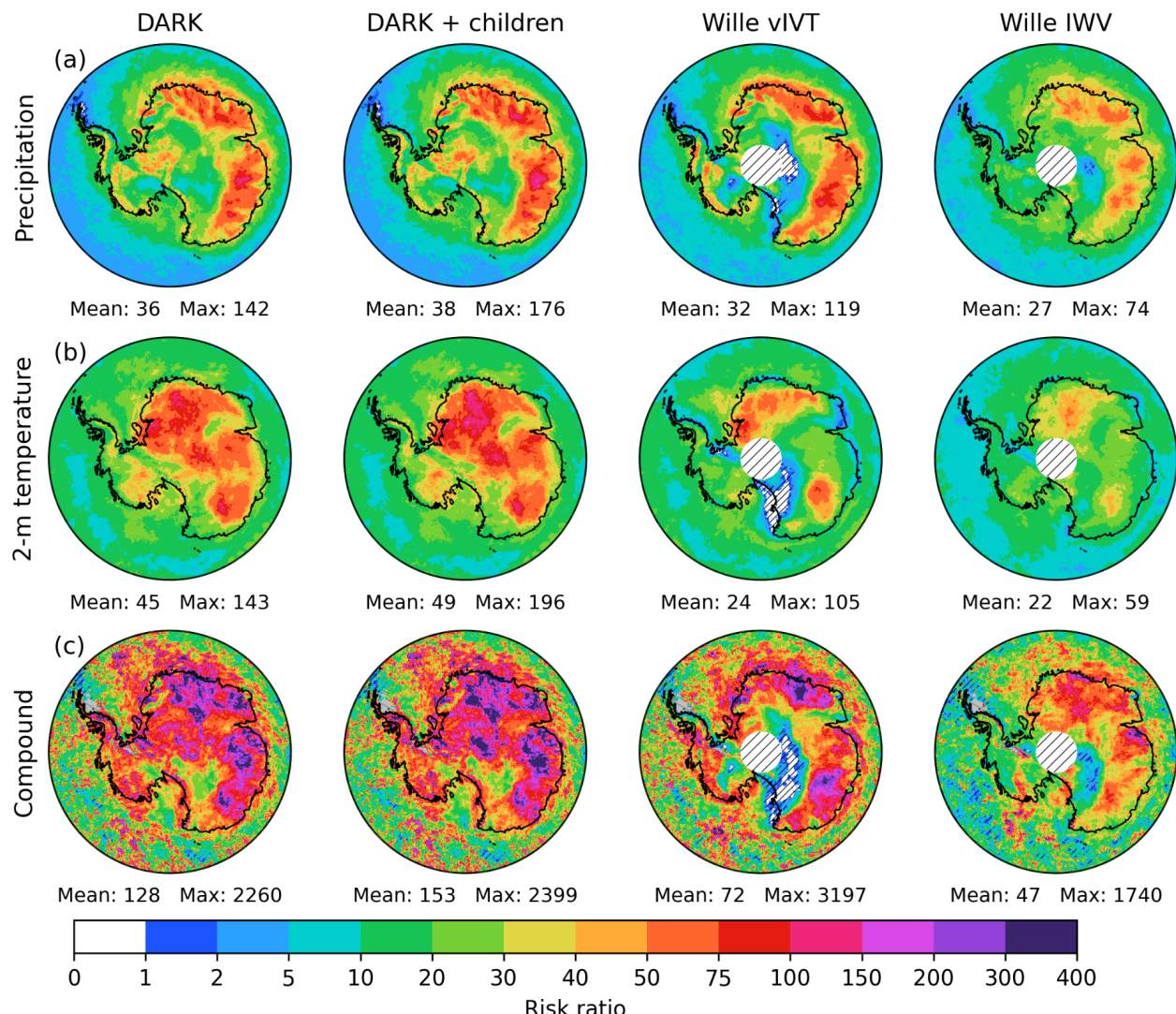


381

382 **Figure 7.** Fraction of compound extreme days combining 99th-percentile precipitation and 2 m air temperature anomalies
383 attributed (Sect. 2.4) to DARK ARs. Row (a) shows DARK ARs and row (b) shows DARK ARs and their children. Columns
384 display (from left to right) the absolute fraction of compound extremes and the differences relative to the Wille vIWT and Wille
385 IWV schemes (percentage points, pp). Antarctic land-only mean and maximum values are reported below each panel. Hatched
386 white areas south of 85° S mark regions without data in the Wille schemes; hatched overlays indicate non-significant values;
387 gray shading indicates grid cells with no detected compound extremes.



388 Risk ratios (RR) are next used to account for differences in AR occurrence frequency (Sect. 2.5). For precipitation, DARK
389 yields RR values comparable to or higher than those of the Wille schemes across most of the AIS (Fig. 8a), indicating that
390 extreme precipitation is about 30 times more likely during an AR, independently from the selected ARDT. The spatial pattern
391 closely resembles that of Wille vIVT, with the highest values north of the EAID and local peaks reaching 142. However, for
392 2 m air temperature (Fig. 8b), the similarity with Wille's ARDTs is weaker. While DARK reproduces the main hotspots seen
393 in Wille's ARDTs, RRs are considerably larger over a much wider area. The Antarctic-wide mean RR reaches 45 (roughly
394 twice the Wille means), with local maxima up to 143, demonstrating that DARK not only amplifies the temperature hotspots
395 detected by Wille vIVT and IWV but also identifies additional regions of strong AR influence beyond those captured by the
396 original scheme. For compound extremes (Fig. 8c), DARK produces a markedly higher RR than Wille's ARDTs, with an
397 Antarctic-wide mean of 128, almost double that of Wille's ARDTs, and local maxima exceeding 10^3 , highlighting the
398 dominant influence of ARs on concurrent warm and wet extremes. Including AR-children further increases both mean and
399 peak RR for precipitation, temperature, and compound events, illustrating that post-landfall moisture remnants can cause
400 extremes after the parent AR loses coherence.



401

402

403

404

405

406

407

Figure 8. Risk ratio (RR; see Sect. 2.5) of 99th-percentile anomalies during AR conditions for (a) 2 m air temperature, (b) precipitation, and (c) compound events (precipitation + temperature; see Sect. 2.4). Columns correspond to DARK ARs, DARK ARs and their children, Wille vIWT, and Wille IWV ARs. Values of RR > 1 indicate an increased likelihood of extremes under AR conditions. Gray areas indicate grid cells without detected compound extremes, hatches indicate non-significant RR (Sect. 2.6).



408

3.4 Regional case studies

409

410 To illustrate the performance of the DARK framework during intense to extreme weather events, we analyze representative
411 cases. The first case study focuses on the McMurdo region, a well-known area situated between the Ross Ice Shelf and Victoria
412 Land, both of which show strong enhancement in DARK relative to Wille's ARDTs. The second case study examines ARs
413 detected south of the EAID, including those crossing the South Pole.

414

415

3.4.1 Extreme events in the McMurdo–Dry Valleys region

416

417

The first case study focuses on the McMurdo–Dry Valleys domain ($160\text{--}168^\circ\text{ E}$, $78.5\text{--}77.5^\circ\text{ S}$),, where two exceptional events exemplify the synoptic conditions driving major precipitation and temperature extremes.

418

419

420

421

422

423

424

425

426

427

428

429

430

431

432

On 1 December 2003 (Fig. 9a), the McMurdo–Dry Valleys region recorded more than 16 mm of precipitation, exceptionally high for this arid environment, representing the largest daily precipitation total in the 1979–2024 ERA5 dataset. Including the following day (2 December 2003, with more than 12 mm, corresponding to the 99.9th percentile), the two day total accounts for over 14 % of the annual precipitation in 2003. The 500-hPa geopotential height anomalies reveal a broad anticyclonic circulation spanning the Antarctic interior from the Bellingshausen Sea to Dome C, with a maximum over Marie Byrd Land. A deep trough northwest of the Ross Sea and another farther north directed a zonal moisture flux from the South Pacific into the western Ross Sea sector. Upon encountering the Transantarctic Mountains, this flux curved equatorward and westward, producing intense coastal precipitation. The DARK scheme captures the full curvature of this moisture filament as it arcs inland over Victoria Land, while neither Wille vIVT nor Wille IWV detect the equatorward-turning portion (Fig. 9a). The precipitation maximum coincides with the AR's interaction with the Transantarctic Mountains, followed by a sharp inland decline in IVT consistent with strong orographic precipitation. By 2 December, the main AR filament had dissipated, leaving behind a remnant classified as an AR-child. Despite its smaller spatial extent, this remnant produced more than 12 mm of precipitation, still within the top 0.1 % of daily values. This demonstrates that post-landfall AR fragments can sustain extreme precipitation even after the parent AR loses coherence. This event highlights the importance of explicitly identifying and tracking AR-children, which can prolong the hydrological impacts of ARs well beyond their formal duration.

433

434

435

436

437

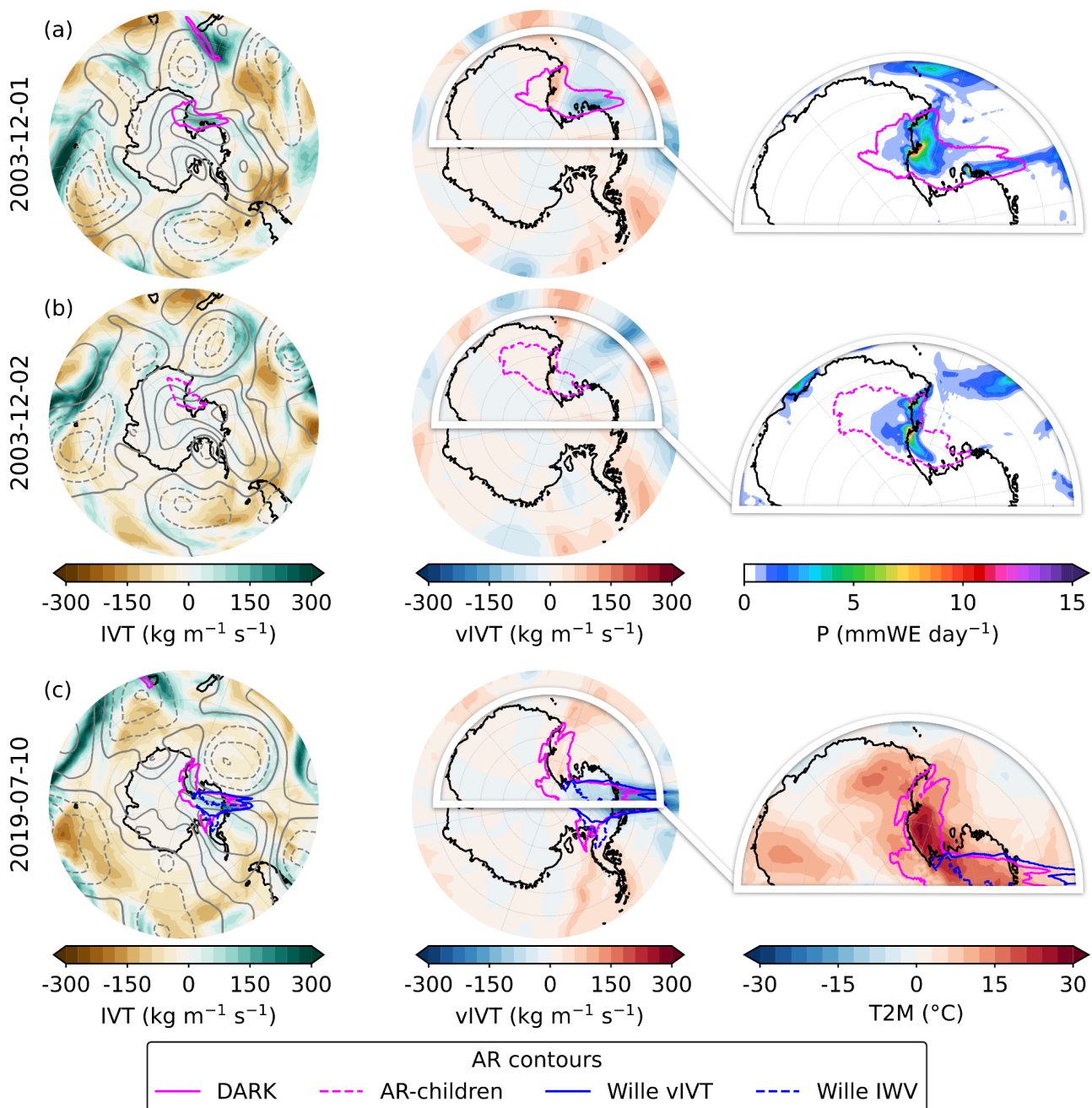
438

439

On 9 July 2019 (Fig. 9b), an exceptional temperature extreme affected the Ross Ice Shelf region, including the McMurdo area, with 2 m air temperature daily anomalies peaking at $+27.9^\circ\text{ C}$ in the McMurdo–Dry Valleys. This event represents the largest daily-mean temperature anomaly in the 1979–2024 ERA5 record, and exceeded $+31^\circ\text{ C}$ over parts of the shelf. The 500-hPa geopotential height anomalies show an extensive anticyclonic structure extending from the southern tip of South America across the Antarctic continent and into the southern Indian Ocean, centered over the Antarctic interior. A deep trough north of the Ross Sea directed moist air from the South Pacific toward the Ross Ice Shelf, where the flow was deflected by the topography of the eastern Ross sector. As the IVT cyclonically curved along the Transantarctic Mountains, leading to



440 equatorward fluxes off the coasts of Victoria Land, the strongest temperature anomalies occurred and peaked over the Ross
441 Ice Shelf. DARK ARs capture the complete curved moisture transport pathway responsible for this event, whereas the Wille
442 schemes detect only the initial southward intrusion and miss the equatorward-turning segment beneath which the peak
443 temperature anomalies occurred.





445 **Figure 9.** Daily composites of the most intense (a–b) precipitation and (c) temperature events in the McMurdo–Dry Valleys
446 region (160–168° E, 78.5–77.5° S). Panels (a) and (b) correspond to 1 and 2 December 2003, respectively, showing the
447 evolution of the same precipitation event, while panel (c) shows the temperature event on 9 July 2019. Each column displays,
448 from left to right: integrated vapor transport (IVT) anomaly ($\text{kg m}^{-1} \text{s}^{-1}$), meridional IVT (vIVT) anomaly ($\text{kg m}^{-1} \text{s}^{-1}$), and (a–
449 b) daily precipitation (mm w.e. day^{-1}) or (c) 2 m air temperature anomaly (°C). Gray contours in the first column indicate 500-
450 hPa geopotential-height anomalies (m; solid = positive, dashed = negative) at 100-m intervals. DARK ARs (solid magenta)
451 and their children (dashed magenta) are shown together with Wille ARs (solid blue = vIVT; dashed blue = IWV). For each
452 day, AR contours represent the maximum spatial extent of each AR type across all 6-hourly time steps (i.e., the union of all
453 detected positions within the day). White-shaded contours in the middle panels outline the domain shown in the rightmost
454 panels.

455 456 3.4.2 ARs reaching the South Pole

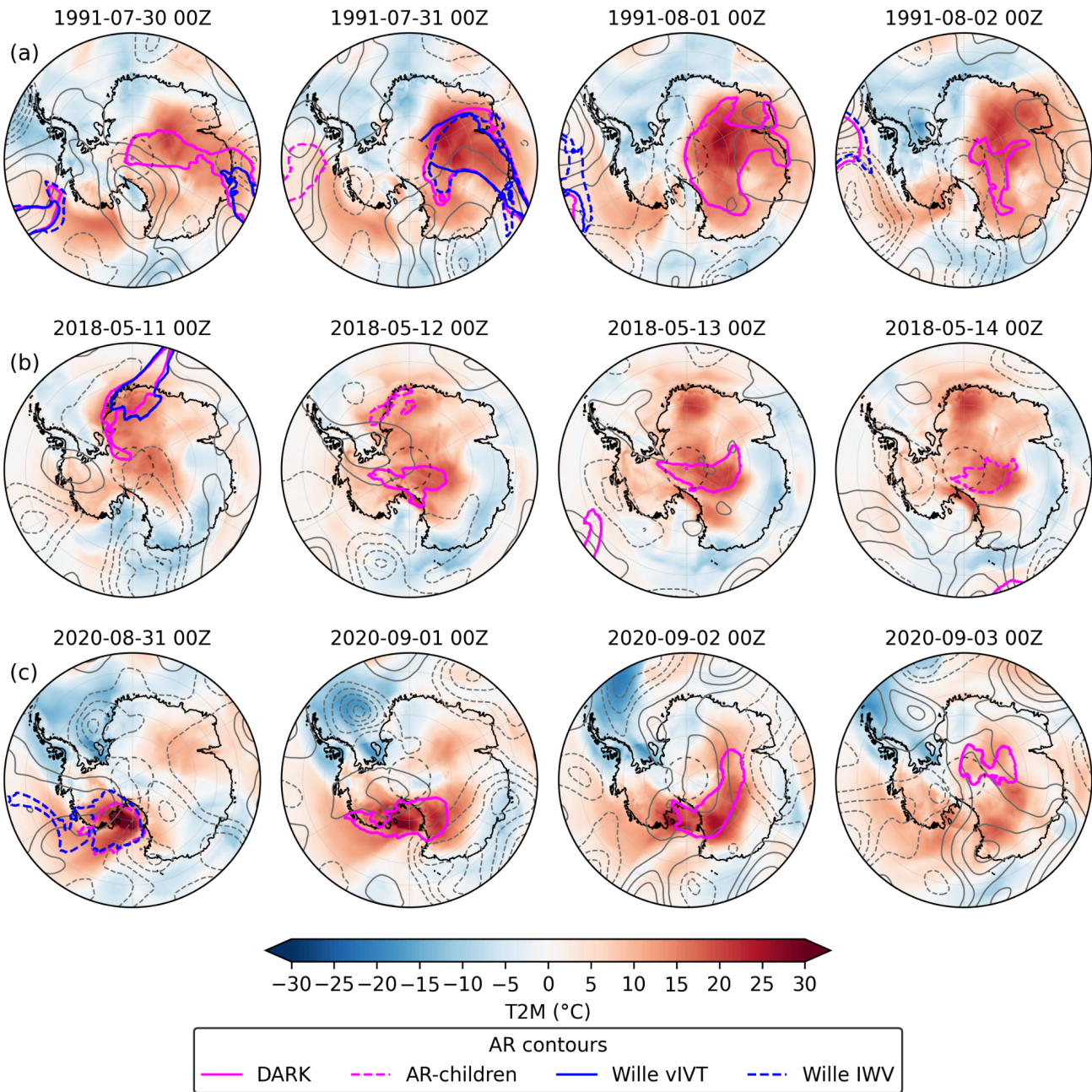
458 One of the major advancements of the DARK framework is its ability to detect ARs reaching the South Pole, whereas previous
459 schemes such as Wille vIVT and IWV ceased detection at 85° S. In ERA5, IVT vectors become ill-defined exactly at 90° S
460 because of the coordinate singularity, which causes an artificial drop in detections at the pole. Nevertheless, DARK captures
461 continuous poleward moisture transport all the way to the South Pole, enabling for the first time a physically consistent
462 identification of ARs in this region. To illustrate this, we examine three events detected by DARK near the pole.

463 On 30 July 1991 (Fig. 10a), a DARK AR was detected extending from the Princess Elizabeth Land coast across the Antarctic
464 interior to the South Pole. The synoptic configuration featured two centers of action, with a low-pressure system east of
465 Princess Elizabeth Land and a high-pressure system farther east, jointly channeling the moisture plume poleward in a roller-
466 like pattern. Both Wille vIVT and DARK identified ARs along this corridor on that day. However, the Wille vIVT AR stopped
467 at the coast as the meridional IVT component weakened below the 98th percentile and the flow turned more zonal toward
468 Dome A and the South Pole. Yet, the total IVT remained strong, allowing DARK to maintain continuous detection inland.
469 Under the AR footprint, 2 m air temperature anomalies already reached around +20 °C, reflecting the strong advection of
470 warm, moist air from lower latitudes. On the following day, the IVT flow advanced farther across the East Antarctic Plateau.
471 Both Wille and DARK detected ARs from the Princess Elizabeth Land coast over Dome A, with their extent broadening to
472 cover areas from Dronning Maud Land to Victoria Land, reaching latitudes as far south as 85° S. Temperature anomalies
473 intensified in step with the AR progression, spreading across the southern flank of the EAID. By the third day, only the DARK
474 AR remained, spanning a broad region south of the EAID and extending to the South Pole, with a tail still visible along the
475 East Antarctic coast. The strongest temperature anomalies, approaching +27 °C, were recorded at this stage beneath and
476 slightly downstream of the AR core. By the fourth day, the feature had contracted into a thinner filament along the southern
477 flank of the EAID, while the residual warm anomalies persisted in the area previously impacted by the main AR.



478 On 11 May 2018 (Fig. 10b), intense moisture transport was directed toward Dronning Maud Land, similarly driven by a marked
479 pressure dipole, with a high-pressure system to the east and a low to the west. Both Wille vIYT and DARK detect ARs in this
480 configuration, but the DARK AR extends farther inland, reaching Queen Elizabeth Land and up to 87° S. This event coincides
481 with widespread positive 2 m air temperature anomalies across most of the Antarctic Ice Sheet, except along the East Antarctic
482 coast from Victoria Land to the Amery Ice Shelf. On the following day, no Wille AR was detected, while the DARK AR had
483 evolved and split into two structures: an AR over the South Pole, just north of the Ross Ice Shelf where surface temperatures
484 continued to rise, and an AR-children along the original AR path over Dronning Maud Land. By the third day, only the main
485 DARK AR remained, now centered over and slightly beyond the South Pole, having crossed the EAID before being deflected
486 westward by the topography. Beneath this AR, 2 m air temperature anomalies intensified further, locally reaching +20 °C. By
487 the fourth day, the AR had decayed into a smaller AR-child, yet the warm anomalies remained strong, particularly within these
488 moisture remnants. Notably, after the AR had moved away from Dronning Maud Land, temperature anomalies there continued
489 to increase through days 3 and 4, suggesting that the warm air mass and its heat content persisted well after the main AR
490 passage.

491 On 31 August 2020 (Fig. 10c), a moisture-laden plume reached the Ross Ice Shelf, similarly guided by a high-pressure system
492 centered over West Antarctica and a low-pressure system over Victoria Land. The non-circular structure of both systems
493 reflects relatively weak wind speeds, which likely explains why this event is not detected by either vIYT or DARK. The event
494 was detected as a Wille IWV AR, extending from the South Pacific across Marie Byrd Land to the Ross Ice Shelf. At its
495 southern tip, a portion of the Wille IWV AR was also classified as an AR-child, indicating sustained, concentrated moisture
496 transport embedded within the broader IWV structure. This episode produced exceptionally strong surface temperature
497 anomalies over the Ross Ice Shelf, locally exceeding +30 °C. On the following day, the anticyclonic anomaly shifted southward
498 toward the South Pole, while the low-pressure system elongated eastward, forming a double-centered trough. Together, these
499 systems established a broad zonal corridor that directed the DARK AR across the Antarctic interior. By the third day, the AR
500 extended along the southern flank of the EAID, maintaining a coherent filament structure. The warm anomalies migrated with
501 the AR core, indicating active advection of heat and moisture along its path. By the fourth day, the AR weakened and contracted
502 into a diminished AR structure centered near the South Pole and extending over southern Dronning Maud Land and southern
503 Princess Elizabeth Land. Despite this decay, pronounced 2 m air temperature anomalies persisted, reflecting the lingering
504 influence of the moist and warm air mass transported deep into the Antarctic interior.



505

506 **Figure 10.** Synoptic evolution of three South-Pole-crossing DARK AR events penetrating south of 85° S. Rows (a–c)
507 correspond to the events from 30 July–2 August 1991, 11–14 May 2018, and 31 August–3 September 2020, respectively.
508 Columns show sequential days at 00 UTC. Filled colors depict 2 m air temperature anomalies ($^{\circ}$ C), and gray contours show
509 500-hPa geopotential-height anomalies (m; solid = positive, dashed = negative) at 50-m intervals. DARK ARs (solid magenta)



510 and their children (dashed magenta) are shown together with Wille ARs (solid blue = vIVT; dashed blue = IWV). The dashed
511 circle marks 85° S, and regions north of 60° S are masked.

512 **4 Discussion & Conclusion**

513 The DARK framework bridges the gap between the intensity-focused Antarctic schemes of Wille vIVT and IWV and the
514 globally applied IVT-based approaches such as Guan and Waliser (2015, 2019), while extending the geometric flexibility
515 recently introduced by Spensberger et al. (2025). Building on Wille's methods, DARK retains the strict 98th-percentile
516 threshold to isolate the most intense moisture-transport events while introducing key advancements: it uses total IVT rather
517 than only its meridional component and computes total filament length instead of meridional extent, thereby removing the
518 directional and geometric constraints that previously limited the detection of curved or equatorward-turning ARs. Global IVT-
519 based schemes such as Guan and Waliser (2015, 2019) also use IVT magnitude but impose a directional coherence constraint
520 that excludes ARs curving or reversing flow direction. By relaxing this requirement, DARK identifies dynamically coherent,
521 non-meridional ARs that are common near the Antarctic coast, where synoptic steering, Coriolis deflection, and topographic
522 deflection distort moisture pathways.

523 Unlike previous frameworks, DARK eliminates the artificial boundary effects that limited AR detection close to the poles. In
524 Wille vIVT, the reversal of the meridional IVT component at the South Pole prevents continuous detection of pole-crossing
525 features, while the 20° meridional extent criterion introduces a secondary edge effect up to about 65° S. The Wille IWV scheme
526 avoids the vIVT singularity but remains affected by this geometric limitation, because it was developed and applied assuming
527 a southward boundary at 85°S. By using total IVT and defining the 2,000 km minimum extent along the full curved axis of the
528 filament rather than its meridional projection, DARK, together with the AR-children add-on, enables continuous tracking of
529 ARs throughout their lifecycle, from oceanic genesis across the Antarctic continent and occasionally the South Pole to their
530 inland decay and fragmentation as AR-children. This provides a seamless representation of poleward moisture transport and
531 its persistence over the ice sheet.

532 The climatology derived from DARK ARs is broadly consistent with that of Wille vIVT and IWV, confirming that it preserves
533 the physical realism of established Antarctic AR frameworks. A majority of Wille ARs are detected by DARK, and overall
534 AR frequency along the Antarctic coast remains similar to that obtained with Wille's schemes, indicating strong agreement to
535 detect the initial moisture intrusions. This shows that the method extends rather than replaces previous approaches: Wille ARs
536 represent some of the most intense events, accounting for much of the precipitation and extreme anomalies. DARK additionally
537 identifies ARs systematically missed by Wille's directional and geometric constraints. These new detections occur mainly
538 south of the EAID, but additional events are found across the continent wherever moisture plumes turn zonally or overturn
539 under the combined influence of vorticity and topography. These ARs are dynamically coherent systems associated with strong
540 precipitation, pronounced temperature anomalies, and compound extremes. Their frequency aligns with the 20 % of



541 extratropical moisture-transport axes that turn equatorward beyond 70° S (Spensberger et al., 2025), although the proportion
542 is smaller here (about 6 %), suggesting that the most intense filaments, such as those detected by Wille, are less likely to
543 overturn than weaker or more diffuse transports. While Wille vIVT remains most effective at isolating direct, intense poleward
544 intrusions, DARK complements it by capturing a broader spectrum of AR geometries that are still physically meaningful and
545 climatically relevant.

546 DARK ARs account for an average of 18 % of total Antarctic precipitation, compared to about 13 % in Wille vIVT. The largest
547 increases occur in coastal embayments and across catchments south of the EAID, where the inclusion of AR-children further
548 amplifies local contributions, raising them from only a few percent in Wille vIVT to over 20 %. This rise does not result from
549 more intense precipitation within individual events but from a higher occurrence and greater diversity of ARs detected by
550 DARK. On average, individual DARK ARs are associated with slightly lower mean precipitation per event than Wille ARs,
551 which remain the most precipitation-intense. However, DARK also identifies additional ARs that are moderately weaker while
552 still belonging to the upper tail of the precipitation distribution. In particular, DARK captures a larger fraction of precipitation
553 extremes, as defined above by the daily 99th-percentile anomaly, with the strongest signals in regions such as McMurdo,
554 Victoria Land, and near the South Pole south of the EAID. A similar pattern emerges for 2 m air temperature and compound
555 extremes, where DARK detects more events than Wille. Risk ratio analysis confirms that this stronger association with
556 extremes is not simply a by-product of higher AR frequency: extreme events are statistically more likely to occur during DARK
557 ARs than during Wille ARs, and even more so when AR-children are included.

558 Another key contribution of this work lies in the introduction of the AR-children module, which extends detection beyond
559 landfall by identifying remnants with high moisture transport that remain dynamically connected to their parent ARs. As ARs
560 encounter the Antarctic coast, condensation, latent heating, and orographic deflection often disrupt their filamentary structure,
561 causing them to fall below the length or coherence thresholds of conventional algorithms. These fragments, although shorter,
562 maintain IVT above the 98th percentile and continue to produce significant precipitation and temperature anomalies inland.
563 The AR-children algorithm captures these post-landfall features, enabling the representation of the decaying yet dynamically
564 active stages of the ARs (Wille et al., 2024). In Antarctica, AR-children are particularly important over Victoria Land and the
565 Amery Ice Shelf, where they account for more than 8 % of total precipitation and contribute up to 20 % of all extreme events,
566 including precipitation, temperature, and compound extremes. When AR-children are included in addition to DARK ARs, the
567 mean association with precipitation extremes increases from 53 % to 58 %, with temperature extremes from 67 % to 71 %,
568 and with compound extremes from 80 % to 83 %. These results demonstrate that AR-children are not marginal phenomena
569 but intrinsic components of the Antarctic AR lifecycle, representing the decaying inland phase of ARs and accounting for their
570 delayed effects on precipitation and temperature extremes.

571 Despite these advances, DARK remains subject to methodological assumptions that introduce uncertainty. A minimum AR
572 length of 2,000 km was imposed to match the typical scale of ARs described in the literature (e.g., Guan and Waliser, 2015;



573 Wille et al., 2021; Skinner et al., 2020; Gorodetskaya et al., 2014), generally longer than 2,000 km and narrower than 1,000
574 km. DARK does not explicitly constrain AR width, as the use of IVT naturally favors elongated structures, in contrast with
575 IWV-based schemes that can produce broad, static moisture plumes. The AR-children module further applies a minimum
576 feature area of 20,000 km² to remove small, short-lived moisture patches. This threshold is not physically based but chosen
577 pragmatically to exclude spurious, localized post-landfall features. These thresholds are empirically motivated by case-study
578 analyses, which show that post-AR moist structures typically extend over at least this spatial scale. While a comprehensive
579 sensitivity analysis is beyond the scope of this study, future work could further explore how varying these thresholds affects
580 detection frequency and precipitation attribution. Likewise, the 15-day rolling window used to compute the 98th-percentile
581 IVT threshold improves upon monthly percentiles by avoiding discontinuities at month boundaries, but it adds complexity that
582 may affect reproducibility. These design choices illustrate the necessary balance between physical robustness and algorithmic
583 simplicity inherent to percentile-based detection frameworks.

584 As with all threshold-based methods, DARK defines discrete events within a continuous moisture field. The 98th-percentile
585 threshold represents both an empirical compromise between inclusiveness and selectivity and a deliberate choice to ensure
586 methodological continuity with previous Antarctic AR frameworks, particularly Wille vIVT and IWV. Lowering the threshold
587 would inflate detections but weaken dynamical coherence, while raising it would isolate too few, overly intense events.
588 Retaining the 98th percentile thus preserves comparability with earlier studies while providing a pragmatic balance that isolates
589 physically meaningful ARs and maintains statistical consistency. Future work could explore adaptive thresholds that evolve
590 with temperature, such as those proposed by Barthélemy et al. (2025) and MacLennan et al. (2025), to better represent
591 thermodynamic scaling under warming conditions and to extend the applicability of DARK and related tools across diverse
592 climate states, from palaeoclimate to future projections.

593 Overall, DARK provides a coherent and physically consistent framework for characterizing Antarctic ARs and their climatic
594 influence. By removing directional and geometric constraints, eliminating artificial boundaries at the pole, and, with the add-
595 on incorporating post-landfall detection through AR-children, it allows continuous tracking of ARs from oceanic genesis to
596 polar dissipation. In doing so, DARK better captures the full lifecycle of Antarctic ARs, from their formation in the lower
597 latitudes, through landfall and inland decay, including a potential passage across the South Pole, thereby providing an
598 unprecedentedly complete view of AR-driven moisture and energy transport over the Antarctic Ice Sheet. In addition to further
599 highlighting the SMB impacts of ARs across the entire Antarctic Ice Sheet as seen here, DARK provides a tool for tracking
600 the influence of residual AR moisture on Antarctic mesoscale-scale atmospheric dynamics like polar lows and barrier jets
601 (Carrasco and Bromwich, 1993; Nigro et al., 2012). This framework bridges global and polar perspectives, linking large-scale
602 moisture transport pathways to regional precipitation, temperature, and compound extremes over the Antarctic Ice Sheet, and
603 highlighting that the influence of ARs extends well beyond their initial landfall.

604 **Code and data availability**



605 The DARK algorithm was developed in Python and is publicly available under an open-source license at
606 https://github.com/victoirebuffet/DARK_atmospheric_river_detection_tool. The detection and analysis scripts rely on
607 standard Python libraries including xarray, numpy, scipy, matplotlib, and cartopy, and are designed to process ERA5 reanalysis
608 data in NetCDF format, however codes were made for MERRA-2 and CESM-LE2, codes are available upon request. ERA5
609 reanalysis data (Hersbach et al., 2023a; Hersbach et al., 2023b) are available from the Copernicus Climate Data Store (CDS)
610 at <https://cds.climate.copernicus.eu/>. The DARK AR catalog is available at <https://doi.org/10.5281/zenodo.17963007>, while
611 the DARK AR+children catalog is available at <https://doi.org/10.5281/zenodo.17962931>. AR catalogs for Wille vIWT and
612 Wille IWV, re-run from the method of Wille et al. (2021), on the full period of study (1979–2023), are available at
613 <https://doi.org/10.5281/zenodo.17968902>.

614 **Author contributions**

615 VB developed the detection algorithms, curated and analyzed the data, and prepared the initial draft of the manuscript,
616 including figures and visualizations. VF and BP guided the investigation, and contributed to refining the final version of the
617 manuscript. JW contributed to the conceptual development of the study, provided scientific guidance throughout the research
618 process, and contributed to revising the final manuscript.

619 **Competing interests**

620 The authors declare that they have no conflict of interest.

621 **Financial support**

622 This research has been supported by the Agence Nationale de la Recherche (ANR) under project ANR-20-CE01-0013
623 (ARCA).

624 **Acknowledgements**

625 We thank the European Centre for Medium-Range Weather Forecasts (ECMWF) for providing the ERA5 reanalysis data. We
626 thank Juliette Blanchet for valuable feedback on the significance testing. We thank the developers of python, matplotlib,
627 cartopy, xarray, scipy, numpy, scikit-image, geopy, netcdf4, networkx and pandas. Calculations were performed using HPC
628 resources from DNUM CCUB (Centre de Calcul de l'Université Bourgogne Europe).



629 **References**

630 Adusumilli, S., A. Fish, M., Fricker, H. A., and Medley, B.: Atmospheric River Precipitation Contributed to Rapid Increases
631 in Surface Height of the West Antarctic Ice Sheet in 2019, *Geophysical Research Letters*, 48, e2020GL091076,
632 <https://doi.org/10.1029/2020GL091076>, 2021.

633

634 American Meteorological Society, Glossary of Meteorology: Atmospheric River.
635 https://glossary.ametsoc.org/wiki/Atmospheric_river, 2024.

636

637 Barthélemy, L., Codron, F., Wille, J., Favier, V., & Clem, K. R.: Future atmospheric rivers in Antarctica: Characteristics and
638 impacts with the IPSL model. *Journal of Geophysical Research: Atmospheres*, 130, e2025JD043398.
639 <https://doi.org/10.1029/2025JD043398>, 2025.

640

641 Carrasco, J. F. and Bromwich, D. H.: Mesoscale cyclogenesis dynamics over the southwestern Ross Sea, Antarctica, *Journal*
642 of *Geophysical Research: Atmospheres*, 98, 12973–12995, <https://doi.org/10.1029/92JD02821>, 1993.

643

644 Chang, E. K. M., Lee, S., and Swanson, K. L.: Storm Track Dynamics, *Journal of Climate*, 15, 2163–2183,
645 [https://doi.org/10.1175/1520-0442\(2002\)015%253C02163:STD%253E2.0.CO;2](https://doi.org/10.1175/1520-0442(2002)015%253C02163:STD%253E2.0.CO;2), 2002.

646

647 Collow, A. B. M., Shields, C. A., Guan, B., Kim, S., Lora, J. M., McClenny, E. E., Nardi, K., Payne, A., Reid, K., Shearer, E.
648 J., Tomé, R., Wille, J. D., Ramos, A. M., Gorodetskaya, I. V., Leung, L. R., O'Brien, T. A., Ralph, F. M., Rutz, J., Ullrich, P.
649 A., and Wehner, M.: An Overview of ARTMIP's Tier 2 Reanalysis Intercomparison: Uncertainty in the Detection of
650 Atmospheric Rivers and Their Associated Precipitation, *Journal of Geophysical Research: Atmospheres*, 127,
651 e2021JD036155, <https://doi.org/10.1029/2021JD036155>, 2022.

652

653 Dacre, H. F. and Clark, P. A.: A kinematic analysis of extratropical cyclones, warm conveyor belts and atmospheric rivers, *npj*
654 *Clim Atmos Sci*, 8, 97, <https://doi.org/10.1038/s41612-025-00942-z>, 2025.

655

656 Gorodetskaya, I. V., Tsukernik, M., Claes, K., Ralph, M. F., Neff, W. D., and Van Lipzig, N. P. M.: The role of atmospheric
657 rivers in anomalous snow accumulation in East Antarctica, *Geophysical Research Letters*, 41, 6199–6206,
658 <https://doi.org/10.1002/2014GL060881>, 2014.

659

660 Gorodetskaya, I. V., Durán-Alarcón, C., González-Herrero, S., Clem, K. R., Zou, X., Rowe, P., Rodriguez Imazio, P., Campos,
661 D., Leroy-Dos Santos, C., Dutrievoz, N., Wille, J. D., Chyhareva, A., Favier, V., Blanchet, J., Pohl, B., Cordero, R. R., Park,
662 S.-J., Colwell, S., Lazzara, M. A., Carrasco, J., Gulisano, A. M., Krakovska, S., Ralph, F. M., Dethinne, T., and Picard, G.:
663 Record-high Antarctic Peninsula temperatures and surface melt in February 2022: a compound event with an intense
664 atmospheric river, *npj Clim Atmos Sci*, 6, 1–18, <https://doi.org/10.1038/s41612-023-00529-6>, 2023.

665

666 Guan, B. and Waliser, D. E.: Detection of atmospheric rivers: Evaluation and application of an algorithm for global studies:
667 *Detection of Atmospheric Rivers*, *J. Geophys. Res. Atmos.*, 120, 12514–12535, <https://doi.org/10.1002/2015JD024257>, 2015.

668



669 Guan, B. and Waliser, D. E.: Tracking Atmospheric Rivers Globally: Spatial Distributions and Temporal Evolution of Life
670 Cycle Characteristics, *Journal of Geophysical Research: Atmospheres*, 124, 12523–12552,
671 <https://doi.org/10.1029/2019JD031205>, 2019.

672

673 Hersbach, H., Bell, B., Berrisford, P., Hirahara, S., Horányi, A., Muñoz-Sabater, J., Nicolas, J., Peubey, C., Radu, R., Schepers,
674 D., Simmons, A., Soci, C., Abdalla, S., Abellán, X., Balsamo, G., Bechtold, P., Biavati, G., Bidlot, J., Bonavita, M., De Chiara,
675 G., Dahlgren, P., Dee, D., Diamantakis, M., Dragani, R., Flemming, J., Forbes, R., Fuentes, M., Geer, A., Haimberger, L.,
676 Healy, S., Hogan, R. J., Hólm, E., Janisková, M., Keeley, S., Laloyaux, P., Lopez, P., Lupu, C., Radnoti, G., De Rosnay, P.,
677 Rozum, I., Vamborg, F., Villaume, S., and Thépaut, J.: The ERA5 global reanalysis, *Quart J Royal Meteorol Soc*, 146, 1999–
678 2049, <https://doi.org/10.1002/qj.3803>, 2020.

679

680 Hersbach, H., Bell, B., Berrisford, P., Biavati, G., Horányi, A., Muñoz Sabater, J., Nicolas, J., Peubey, C., Radu, R., Rozum,
681 I., Schepers, D., Simmons, A., Soci, C., Dee, D., Thépaut, J-N.: ERA5 hourly data on pressure levels from 1940 to present.
682 Copernicus Climate Change Service (C3S) Climate Data Store (CDS), DOI: [10.24381/cds.bd0915c6](https://doi.org/10.24381/cds.bd0915c6), 2023a.

683

684 Hersbach, H., Bell, B., Berrisford, P., Biavati, G., Horányi, A., Muñoz Sabater, J., Nicolas, J., Peubey, C., Radu, R., Rozum,
685 I., Schepers, D., Simmons, A., Soci, C., Dee, D., Thépaut, J-N. : ERA5 hourly data on single levels from 1940 to present.
686 Copernicus Climate Change Service (C3S) Climate Data Store (CDS) : [10.24381/cds.adbb2d47](https://doi.org/10.24381/cds.adbb2d47), 2023b.

687

688 Katz, D., Baptista, J., Azen, S. P., and Pike, M. C.: Obtaining Confidence Intervals for the Risk Ratio in Cohort Studies,
689 *Biometrics*, 34, 469–474, <https://doi.org/10.2307/2530610>, 1978.

690

691 Maclennan, M. L., Lenaerts, J. T. M., Shields, C., and Wille, J. D.: Contribution of Atmospheric Rivers to Antarctic
692 Precipitation, *Geophysical Research Letters*, 49, e2022GL100585, <https://doi.org/10.1029/2022GL100585>, 2022.

693

694 Maclennan, M. L., Winters, A. C., Shields, C. A., Thaker, R., Barthelemy, L., Codron, F., and Wille, J. D.: Rising atmospheric
695 moisture escalates the future impact of atmospheric rivers in the Antarctic climate system, *Commun Earth Environ*, 6, 369,
696 <https://doi.org/10.1038/s43247-025-02333-x>, 2025.

697

698 Mattingly, K. S., Mote, T. L., and Fettweis, X.: Atmospheric River Impacts on Greenland Ice Sheet Surface Mass Balance,
699 *Journal of Geophysical Research: Atmospheres*, 123, 8538–8560, <https://doi.org/10.1029/2018JD028714>, 2018.

700

701 Nigro, M. A., Cassano, J. J., Lazzara, M. A., and Keller, L. M.: Case Study of a Barrier Wind Corner Jet off the Coast of the
702 Prince Olav Mountains, Antarctica, *Monthly Weather Review*, 140, 2044–2063, <https://doi.org/10.1175/MWR-D-11-00261.1>,
703 2012.

704

705 Skinner, C. B., Lora, J. M., Payne, A. E., and Poulsen, C. J.: Atmospheric river changes shaped mid-latitude hydroclimate
706 since the mid-Holocene, *Earth and Planetary Science Letters*, 541, 116293, <https://doi.org/10.1016/j.epsl.2020.116293>, 2020.

707



708 Spensberger, C., Konstali, K., and Spengler, T.: Moisture transport axes: a unifying definition for tropical moisture exports,
709 atmospheric rivers, and warm moist intrusions, *Weather and Climate Dynamics*, 6, 431–446, <https://doi.org/10.5194/wcd-6-431-2025>, 2025.

711

712 Turner, J., Phillips, T., Thamban, M., Rahaman, W., Marshall, G. J., Wille, J. D., Favier, V., Winton, V. H. L., Thomas, E.,
713 Wang, Z., van den Broeke, M., Hosking, J. S., and Lachlan-Cope, T.: The Dominant Role of Extreme Precipitation Events in
714 Antarctic Snowfall Variability, *Geophysical Research Letters*, 46, 3502–3511, <https://doi.org/10.1029/2018GL081517>, 2019.

715

716 Wille, J. D., Favier, V., Dufour, A., Gorodetskaya, I. V., Turner, J., Agosta, C., and Codron, F.: West Antarctic surface melt
717 triggered by atmospheric rivers, *Nat. Geosci.*, 12, 911–916, <https://doi.org/10.1038/s41561-019-0460-1>, 2019.

718

719 Wille, J. D., Favier, V., Gorodetskaya, I. V., Agosta, C., Kittel, C., Beeman, J. C., Jourdain, N. C., Lenaerts, J. T. M., and
720 Codron, F.: Antarctic Atmospheric River Climatology and Precipitation Impacts, *Journal of Geophysical Research: Atmospheres*, 126, <https://doi.org/10.1029/2020jd033788>, 2021.

721

722 Wille, J. D., Favier, V., Jourdain, N. C., Kittel, C., Turton, J. V., Agosta, C., Gorodetskaya, I. V., Picard, G., Codron, F.,
723 Santos, C. L.-D., Amory, C., Fettweis, X., Blanchet, J., Jomelli, V., and Berchet, A.: Intense atmospheric rivers can weaken
724 ice shelf stability at the Antarctic Peninsula, *Commun Earth Environ*, 3, 1–14, <https://doi.org/10.1038/s43247-022-00422-9>,
725 2022.

726

727 Wille, J. D., Pohl, B., Favier, V., Winters, A. C., Baiman, R., Cavallo, S. M., Leroy-Dos Santos, C., Clem, K., Udy, D. G.,
728 Vance, T. R., Gorodetskaya, I., Codron, F., and Berchet, A.: Examining Atmospheric River Life Cycles in East Antarctica,
729 *Journal of Geophysical Research: Atmospheres*, 129, e2023JD039970, <https://doi.org/10.1029/2023JD039970>, 2024.

730

731 Wille, J. D., Favier, V., Gorodetskaya, I. V., Agosta, C., Baiman, R., Barrett, J. E., Barthelemy, L., Boza, B., Bozkurt, D.,
732 Casado, M., Chyhareva, A., Clem, K. R., Codron, F., Datta, R. T., Durán-Alarcón, C., Francis, D., Hoffman, A. O., Kolbe, M.,
733 Krakovska, S., Linscott, G., MacLennan, M. L., Mattingly, K. S., Mu, Y., Pohl, B., Santos, C. L.-D., Shields, C. A., Toker, E.,
734 Winters, A. C., Yin, Z., Zou, X., Zhang, C., and Zhang, Z.: Atmospheric rivers in Antarctica, *Nat Rev Earth Environ*, 6, 178–
735 192, <https://doi.org/10.1038/s43017-024-00638-7>, 2025.

736

737 Wirth, V., Riemer, M., Chang, E. K. M., and Martius, O.: Rossby Wave Packets on the Midlatitude Waveguide—A Review,
738 *Monthly Weather Review*, 146, 1965–2001, <https://doi.org/10.1175/MWR-D-16-0483.1>, 2018.

739

740 Zhu, Y. and Newell, R. E.: A Proposed Algorithm for Moisture Fluxes from Atmospheric Rivers, *Monthly Weather Review*,
741 126, 725–735, [https://doi.org/10.1175/1520-0493\(1998\)126%253C0725:APAFMF%253E2.0.CO;2](https://doi.org/10.1175/1520-0493(1998)126%253C0725:APAFMF%253E2.0.CO;2), 1998.

742

743

744